ADVANCED OPTICAL MATERIALS
www.advopticalmat.de

A Ho^{3+}-Based Luminescent Thermometer for Sensitive Sensing over a Wide Temperature Range

Thomas P. van Swieten, Dechao Yu, Ting Yu, Sander J. W. Vonk, Markus Suta, Qinyuan Zhang, Andries Meijerink, and Freddy T. Rabouw**

Luminescence thermometry is used in a variety of research fields for non-invasive temperature sensing. Lanthanide-doped micro-/nanocrystals are exceptionally suitable for this. The popular concept of luminescence-intensity-ratio thermometry is based on emission from thermally coupled levels in a single lanthanide ion, following Boltzmann's law. These thermometers can measure temperature with low uncertainty, but only in a limited temperature range. In this work, a Ho^{3+}-based thermometer is presented and quantitatively modeled with sustained low temperature uncertainty from room temperature up to 873 K. The thermometer shows bright green and red luminescence with a strong and opposite dependence on temperature and Ho^{3+} concentration. This is the result of temperature-dependent competition between multi-phonon relaxation and energy transfer, feeding the green- and red-emitting levels, respectively, following excitation with blue light. This simple and quantitative model of this competition predicts the output spectrum over a wide range of temperatures (300–873 K) and Ho^{3+} concentrations (0.1–30%). The optimum Ho^{3+} concentration can thus be determined for reliable measurements over any temperature range of interest. Quantitative modeling as presented here is crucial to optimally benefit from the potential of energy-transfer thermometers to achieve low measurement uncertainties over a wide temperature range.

1. Introduction

In many research fields, ranging from cell biology to catalysis, the size and invasiveness of conventional thermometers hinders accurate temperature sensing.[1,2] Remote temperature sensing based on luminescence thermometry offers an alternative that is capable of measuring heat generation and diffusion on the microscopic scale.[3] Among the various choices of luminescent systems,[4–9] crystals doped with lanthanide (Ln^{3+}) ions represent a particularly promising class of luminescent thermometers, because their dimensions can be tuned from a few nanometers to several micrometers and their photoluminescence spectrum is sensitive to temperature. A characteristic feature of Ln^{3+} ions is their rich energy level structure, which results in emission spectra with well-separated lines. Typically, the luminescence intensity ratio (LIR) between two of these emission lines is used as a sensitive measure for the temperature of the Ln^{3+}-doped crystal. After insertion of these ratiometric thermometers into a system of interest, remote operation simply involves excitation by light and detection of the luminescence with standard spectroscopic equipment.

The performance of a ratiometric thermometer is determined by how sensitively the LIR reacts to temperature. In general, the performance at a given temperature (T) is quantified in terms of the relative sensitivity[10]

$$S_r = \frac{1}{\mathrm{LIR}}\left|\frac{\mathrm{dLIR}}{\mathrm{d}T}\right| \quad (1)$$

with units of (% K^{-1}). A high relative sensitivity allows for accurate probing of small temperature differences. In addition, a reliable temperature measurement requires high precision, which depends on the signal-to-noise ratio of the measurement.[11,12] The precision improves with longer acquisition time and higher brightness of the thermometer. The multitude of temperature-dependent emission lines from Ln^{3+} ions offers many possibilities to optimize sensitivity and precision for the temperature range of interest. The search for superior accuracies has already led to the development of a large variety of ratiometric thermometers.[10]

A popular class of ratiometric thermometers relies on thermal coupling between two excited states of individual Ln^{3+} dopants. The LIR of the emission lines from the two states follows Boltzmann statistics, as long as thermal coupling between them is much faster than radiative decay.[13] The relative sensitivity for

T. P. van Swieten, Dr. D. Yu, Dr. T. Yu, S. J. W. Vonk, Dr. M. Suta, Prof. A. Meijerink, Dr. F. T. Rabouw
Debye Institute for Nanomaterials Science
Utrecht University
Princetonplein 1, Utrecht 3584CC, The Netherlands
E-mail: d.yu@uu.nl; f.t.rabouw@uu.nl
Dr. D. Yu, Dr. T. Yu, Prof. Q. Zhang
State Key Laboratory of Luminescent Materials and Devices
Institute of Optical Communication Materials
South China University of Technology
Guangzhou 510641, P. R. China
The ORCID identification number(s) for the author(s) of this article can be found under https://doi.org/10.1002/adom.202001518.

DOI: 10.1002/adom.202001518

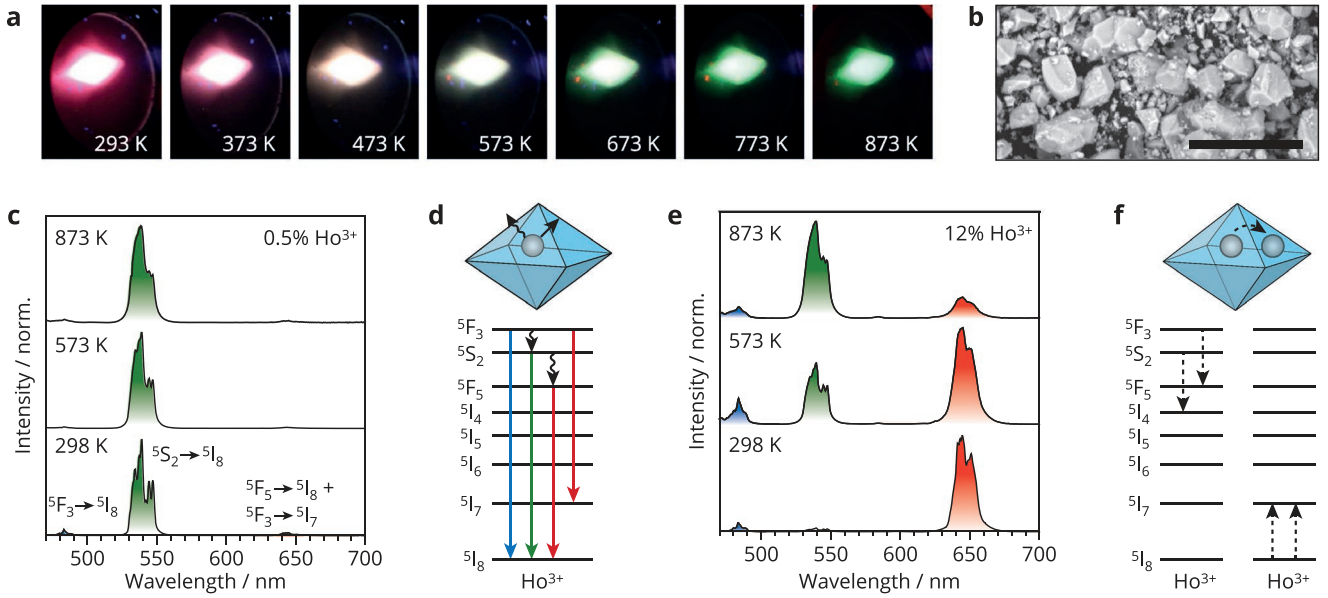

Figure 1. Ho^{3+} as a thermometer based on cross-relaxation. a) Photographs of the $Na(Y,Gd)F_4$ thermometer material doped with 12%-doped Ho^{3+} sample at various temperatures upon excitation with 358 nm. b) Scanning electron micrographs of the 12%-doped Ho^{3+} sample. The scale bar corresponds to 10 µm. c) Emission spectra of the 0.5%-doped Ho^{3+} sample at various temperatures upon excitation with a 450 nm laser. The dominant green luminescence around 540 nm is due to the $^5F_4,^5S_2 \rightarrow {}^5I_8$ transition. The blue emission around 485 nm is due to $^5F_3 \rightarrow {}^5I_8$ transition and the red emission centered around 640 nm is due to the overlapping $^5F_5 \rightarrow {}^5I_8$ and $^5F_3 \rightarrow {}^5I_7$ transitions. d) Energy level diagram of a single Ho^{3+} ion.[22] The wavy arrows represent multi-phonon relaxation and the straight arrows correspond to radiative decay. For more details of the energy level structure of Ho^{3+} in $Na(Y,Gd)F_4$, including the energy gaps between the different levels, Figure S3, Supporting Information. e) Emission spectra of the 12%-doped Ho^{3+} sample at various temperatures. f) Energy level diagram of an excited and a ground-state Ho^{3+} ion. The dashed arrows represent cross-relaxation from the blue- or the green-emitting level of an excited Ho^{3+} ion, populating the $^5I_7$ level in a nearby Ho^{3+} ion that was initially in the $^5I_8$ ground state.

such "Boltzmann thermometers" follows a simple analytical dependence on temperature of $S_r = \Delta E/k_B T^2$, where ΔE is the energy separation between the coupled states. This relation reveals a fundamental limitation of the Boltzmann thermometer: they offer low relative sensitivities at high temperatures ($k_B T > \Delta E$) because the Boltzmann populations of the two coupled states are nearly equal. On the other hand, the measurement precision is low at lower temperatures ($k_B T < \Delta E$) because the population of the upper level is negligible. Accurate and precise temperature sensing over a wide range thus requires a ratiometric thermometer with an alternative working mechanism.[14,15]

Alternative ratiometric thermometers typically consist of a material doped with different Ln^{3+} ions, e.g., Eu^{3+} and Tb^{3+}, that are connected by energy-transfer pathways with a strong temperature dependence.[16–18] This operating mechanism does not lead to a thermal equilibrium of excited-state populations, which makes higher relative sensitivities with yet appreciable luminescence intensities from the different ions possible.[19,20] Recently, Ximendes et al. reported a similar concept using LaF_3 nanoparticles doped with high concentrations of Tm^{3+}, which showed cross-relaxation (i.e., partial energy transfer between two identical ions).[21] However, the working mechanism of energy-transfer thermometers is complicated because it does not only depend on relaxation processes within an ion but also involves interactions between different ions. Consequently, it has not yet been possible to develop a quantitative method that predicts the accuracy and the precision of energy-transfer thermometers.

In this work, we introduce a Ho^{3+}-based cross-relaxation thermometer, measure its temperature-dependent luminescence, and quantitatively model its performance. Our thermometer operates via the competition between a temperature- and a doping-concentration-dependent decay pathway that lead to green and red emission, respectively. We construct a quantitative model for the rates and efficiencies of the complex set of decay pathways involved as a function of temperature and Ho^{3+} concentration. This model successfully predicts the red-to-green LIR as well as the accuracy and the precision of temperature measurements. It can thus serve as a design tool to calculate the Ho^{3+} concentration that enables the most reliable temperature measurements for any temperature regime of interest. Our method of thermometer evaluation is an important step for the design of new energy-transfer thermometers focused on and optimized for the desired application.

2. Results

Figure 1a demonstrates the potential of our Ho^{3+}-based thermometer, reflected by the strong color shift with increasing temperature going from red through white to green.[23–26] Specifically, we prepared microcrystalline fluoride compounds doped with different concentrations of Ho^{3+}, i.e., β-$NaY_{0.75-x}Gd_{0.25}Ho_xF_4$ (Figure 1b).[27] Excitation of these samples with 450 nm light results in a blue, a green, and a red emission band, which are due to the $^5F_3 \rightarrow {}^5I_8$, $^5F_4,^5S_2 \rightarrow {}^5I_8$, and $^5F_5 \rightarrow {}^5I_8 + {}^5F_3 \rightarrow {}^5I_7$ radiative transitions respectively.[28] Competition between different temperature-dependent decay pathways of an excited Ho^{3+} ion, including energy-transfer

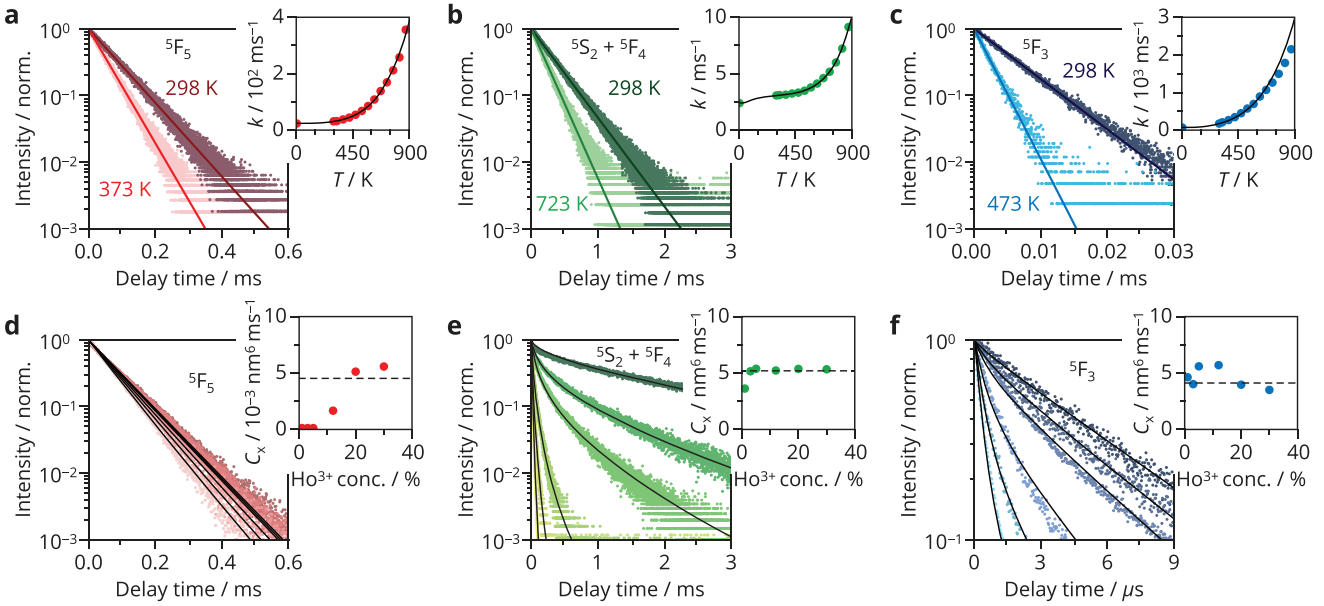

Figure 2. Quantification of radiative decay, multi-phonon relaxation, and cross-relaxation. a) Decay curves of the red-emitting level ($^5F_5$) measured at 645 nm upon resonant excitation at 638 nm of the 0.1%-doped Ho^{3+} sample, at two different temperatures chosen to illustrate the effect of multi-phonon relaxation. The solid lines are fits to a model of single-exponential decay. The inset shows the decay rates obtained from the fits at various temperatures. The black line is a fit to a model of temperature-dependent multi-phonon relaxation. b) Same as in panel (a) but for the green-emitting level ($^5S_2 + {}^5F_4$) measured at 542 nm upon excitation at 535 nm. The black line is a fit to a model of temperature-dependent multi-phonon relaxation and thermal equilibrium between $^5S_2$ and $^5F_4$ populations. c) Same as in panel (b) but for the blue-emitting level ($^5F_3$) measured at 487 nm upon excitation at 447 nm and thermal equilibrium between $^5F_3$, $^5F_2$, and $^3K_8$ populations. d) Decay curves of the red-emitting level measured at room temperature upon resonant excitation of samples with different Ho^{3+} concentrations (0.5%, 1%, 3%, 5%, 12%, 20%, and 30% with decreasing darkness of the color). The solid lines show the results of a global fit of all decay curves to a model of cross-relaxation providing one value for the "cross-relaxation strength" C_x (dashed line in the inset). The C_x values in the inset are the result of fits of the individual decay curves to the cross-relaxation model. e) Same as in panel (d) but for the green-emitting level. f) Same as in panel (d) but for the blue-emitting level.

pathways between neighboring Ho^{3+} ions, controls the relative intensity of these emission lines. To quantitatively understand and predict the performance of our Ho^{3+}-based thermometer, we performed a systematic analysis of these various decay pathways and their temperature dependence.

First, we analyze the luminescence at low Ho^{3+} concentration, at which the ion-to-ion distances in the crystal are large and energy-transfer interactions between ions are thus negligible. In this concentration regime (≤ 0.5%), relaxation from the blue-emitting ($^5F_3$), green-emitting ($^5S_2 + {}^5F_4$), and red-emitting ($^5F_5$) levels of Ho^{3+} takes place only via radiative decay or multi-phonon relaxation, i.e., coupling to phonons of the host lattice to bridge the energy gap between levels. Phonon-mode occupations increase with increasing temperature, which results in faster multi-phonon relaxation. In the emission spectra of the 0.5%-doped Ho^{3+} sample following excitation at 450 nm (Figure 1c), we observe intense luminescence at 540 nm, indicating that multi-phonon relaxation to the green-emitting level followed by radiative decay is the dominant relaxation process (Figure 1d). The small energy gap ΔE between the blue- and the green-emitting level (2000 cm^{-1}) already suggested that emission of only four to six phonons in a hexagonal fluoride host can effectively bridge this gap.[22,29,30] Besides a weak blue emission, we notice a weak red emission that results from a combination of multi-phonon relaxation from the green- to the red-emitting level over a larger 3000 cm^{-1} energy gap, cross-relaxation from the blue- to the red-emitting level, and red emission from the blue-emitting level to the first excited Ho^{3+} level $^5I_7$ (Zou et al.[25] and Figure S4, Supporting Information). Increasing temperature causes only a slight change of the luminescence spectrum (Figure 1c), reflecting poor thermometer performance at low Ho^{3+} concentration. At the same time, this confirms that our thermometer is stable at elevated temperatures up to 873 K, as changes of the host crystal structure would affect emission peak positions and line shapes.

An increase of the Ho^{3+} concentration decreases the distance between ions and thus makes ion–ion interactions such as cross-relaxation more likely. The red color in the photographs of the 12%-doped Ho^{3+} sample at room temperature (Figure 1a) already hinted towards an efficient pathway to populate the red-emitting level in samples with higher Ho^{3+} concentrations. Instead of a dominant green luminescence observed at low Ho^{3+} concentrations (Figure 1c), the emission spectra of the 12%-doped Ho^{3+} sample (Figure 1e) indeed show a strong red emission as compared to the blue and green emissions, at low temperature. Based on the energy level structure of Ho^{3+} (Figure 1f),[31] cross-relaxation from the blue- to the red-emitting level can explain the strong red emission. The drastic increase of the green luminescence at elevated temperatures is due to faster blue-to-green multi-phonon relaxation competing with temperature-independent cross-relaxation that feeds the red-emitting level, as we quantify in detail below (**Figure 2**). Such a temperature-dependent change of the dominant decay pathways is beneficial for a high relative sensitivity of the

thermometer. An increase of the Ho^{3+} concentration from 12% to 30% further changes the luminescence and its response to temperature (Figure S1, Supporting Information). Overall, these observations clearly indicate that the Ho^{3+} concentration is the key parameter to optimize thermometer performance for the temperature range of interest.

Rational optimization of the Ho^{3+} concentration for a specific temperature range requires a quantitative model that accounts for the efficiencies of radiative decay, multi-phonon relaxation, and cross-relaxation. Our first step in the development of such a model was to analyze the effect of temperature on the decay pathways in isolated ions, i.e., radiative decay and multi-phonon relaxation. Figure 2a–c shows decay curves at a Ho^{3+} concentration of 0.1% for the red-, the green-, and the blue-emitting level, respectively. The curves follow single-exponential decay at all temperatures. This is a clear indication for the absence of interactions between Ho^{3+} ions, since this would lead to multi-exponential decay. The total decay rate $k(T)$ increases with increasing temperature as

$$k(T) = k_r + k_{nr}\left[1 + n(T)\right]^{\Delta E/\hbar\omega_{vib}} \quad (2)$$

Here, the radiative rate k_r is assumed constant with temperature, which is an excellent approximation in the case of lanthanides, while the nonradiative contribution depends on the zero-temperature multi-phonon relaxation rate k_{nr}, the phonon occupation $n(T)$, the effective energy $\hbar\omega_{vib}$ of the phonons involved, and the number of phonons needed to bridge the energy gap ($\Delta E/\hbar\omega_{vib}$).[32–34] In the inset of Figure 2a, we fit the temperature dependence of the decay rates from the red-emitting level to Equation (2). The fit matches the data well, yielding a fitted phonon energy of 360 cm^{-1}, which corresponds well to the expected value for hexagonal fluoride lattices.[29] Notably, we included a decay measurement at 4 K in the fitting procedure to ensure reliable values for k_r and k_{nr}. Similar procedures yield models for radiative decay and multi-phonon relaxation from the green- and the blue-emitting levels (Figure 2b–c; Discussion S1, Supporting Information).[13,33,35] Multi-phonon relaxation from the blue- and from the red-emitting level are both fast. Multi-phonon relaxation from the green-emitting level is slower, sets in at higher temperature, and shows a sharper onset than multi-phonon relaxation from the blue- and red-emitting level. This difference is caused by the larger energy gap that the green-emitting level must bridge in multi-phonon relaxation and explains the dominant green luminescence in samples with a low Ho^{3+} concentration. This explains the dominant green luminescence of samples with a low Ho^{3+} concentration (Figure 1c). Besides this qualitative observation, our analysis also enabled a quantitative description of the temperature-dependent decay pathways in individual Ho^{3+} ions.

The next step is the quantification of cross-relaxation in samples with higher Ho^{3+} concentration. In general, cross-relaxation is a type of Förster resonance energy transfer via electric dipole to electric dipole coupling. The cross-relaxation rate k_x scales with the distance R between an excited Ho^{3+} donor ion and a ground-state Ho^{3+} acceptor ion as $k_x = C_x R^{-6}$. Herein C_x is the "cross-relaxation strength" that depends, among other parameters, on the spectral overlap between the donor and acceptor transitions.[32] Figure 2d–f shows the effect of cross-relaxation on the decay dynamics from the red-, green-, and blue-emitting levels, respectively. At a fixed temperature (298 K), decay becomes faster with increasing Ho^{3+} concentration. The decay curves of the green- and blue-emitting levels are multi-exponential at high concentrations, which is a signature of ion–ion interactions over a distribution of distances R. While these observations are a clear demonstration of cross-relaxation, the strength of cross-relaxation is different for the three levels. Specifically, the decay of the green- and blue-emitting levels (Figure 2e,f) accelerates much more strongly with increasing Ho^{3+} concentration than that of the red-emitting level (Figure 2d). Close resonance of the $^5I_8 \rightarrow {}^5I_7$ acceptor transition with donor transitions from the green- and blue-emitting levels (Figure 1f) explains this observation. No such resonance is present for cross-relaxation from the red-emitting level resulting in $\approx 10^3$ times lower value of C_x.

To model cross-relaxation quantitatively, we explicitly account for the distribution of discrete ion-to-ion distances R that occur when Ho^{3+} ions randomly occupy lattice sites of the host crystal at a certain doping concentration using our shell model (Discussion S1, Supporting Information).[36–38] The only free parameter in our model is the cross-relaxation strength C_x, the value of which we determine by fitting the experimental data for varying Ho^{3+} concentration (Figure 2d–f). The photoluminescence decay curves of the blue-emitting level contain a weak slow component that we excluded from the fitting procedure (Figure S6, Supporting Information). For our analysis, we first fitted the individual curves separately, which resulted in a separate estimate for C_x for each Ho^{3+} concentration. In the insets of Figure 2d–f, we compare these separate estimates for C_x with a global fitting procedure that includes all decay curves at different Ho^{3+} concentrations, yielding a single value for C_x. The solid black lines through the decay curves show the results of the global fits. Our model captures how cross-relaxation causes faster decay for increasing Ho^{3+} concentration. A similar analysis at elevated temperatures indicates that the rates of cross-relaxation from the three levels are insensitive to temperature (Figure S7, Supporting Information). Therefore, we use the C_x values from the global fits to describe cross-relaxation interactions between Ho^{3+} ions at all temperatures.

Our cross-relaxation thermometer relies on the effect of temperature on the blue, the green, and the red luminescence intensities (**Figure 3**a). The analysis of the decay dynamics showed that the blue-emitting level undergoes fast depopulation by two competing processes. One of them is multi-phonon relaxation to the green-emitting level, which is sensitive to temperature. The other process is cross-relaxation to the red-emitting level, which depends on the Ho^{3+} concentration. The green-emitting level is relatively unaffected by multi-phonon relaxation but experiences fast decay via cross-relaxation to the $^5I_4$ level.[31] However, this does not influence the population of the blue- or the red-emitting level. The red-emitting level is only weakly affected by multi-phonon relaxation and cross-relaxation. Competition between multi-phonon relaxation and cross-relaxation from the blue-emitting level is thus the most important contribution to color changes with temperature and Ho^{3+} concentration (Figure S8, Supporting Information). This determines the working mechanism of our thermometer.

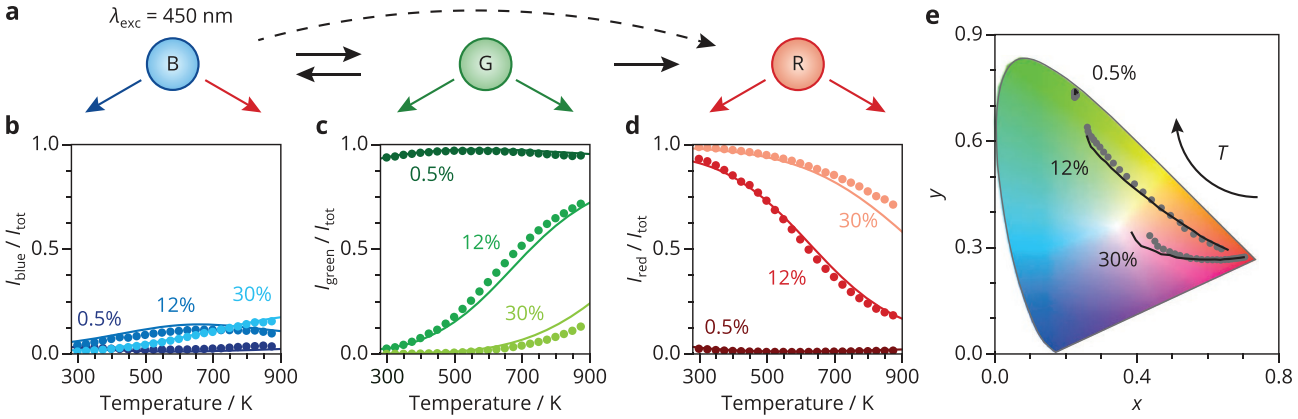

Figure 3. Comparison of the calculated and the experimental emission intensities. a) A simplified schematic of the relevant feeding mechanisms to calculate the efficiency of radiative decay (solid colored arrows) from $^5F_3$ (B), $^5S_2$ + $^5F_4$ (G), and $^5F_5$ (R) levels. Multi-phonon relaxation (solid black arrow) and cross-relaxation (dashed black arrow) connect these levels (Figure S6, Supporting Information, for the complete scheme). Comparison of the experimentally measured (dots) and the calculated (lines) relative intensities of b) the blue, c) the green, and d) the red emissions as a function of temperature for three different Ho^{3+} concentrations. The experimental relative intensities were determined by integrating the emission spectra between 460–500 nm, 515–575 nm, and 625–670 nm, respectively. e) The CIE 1931 diagram plotted with the experimentally measured (dots) and the calculated (lines) color coordinates at various temperatures for three different Ho^{3+} concentrations.

To evaluate the performance of our thermometer, we first construct a model that calculates the relative emission intensities of the blue-, green-, and red-emitting level. This model takes all relevant decay pathways into account (Figure 3a) to determine the efficiencies of radiative decay and combines these with the branching ratios of the transitions to the ground state ($^5I_8$). These efficiencies depend on the rates of radiative decay, temperature-dependent multi-phonon relaxation, and the Ho^{3+}-concentration-dependent cross-relaxation. We obtained these parameters, which we need as an input for our model, from the analysis of Figure 2 (Discussion S2, Supporting Information).[39] In this way, we are able to predict the emission color of our thermometer for any arbitrary temperature and Ho^{3+} concentration.

As a test of our model, Figure 3b–e compares the calculated blue, green, and red emission intensities with the experimentally measured intensities. We observe an overall match between the calculated and the measured intensities, which validates this model as a basis for quantitative thermometer evaluation. As observed in the experimental spectra (Figure 1c,e; Figure S1, Supporting Information), the blue intensity is weak over the whole temperature range and for all concentrations due to strong competition of multi-phonon relaxation and cross-relaxation with radiative decay. The effect of temperature and concentration is more pronounced for the green and the red intensity—they even follow opposite trends. At low temperatures, high Ho^{3+} concentrations cause a weak green emission and a strong red emission because cross-relaxation dominates over multi-phonon relaxation within the blue level. Elevated temperatures compensate this effect, since they enhance multi-phonon relaxation leading to an increase of the green intensity and a decrease of the red intensity. We attribute the small difference between the measured and calculated intensities for the 30%-doped Ho^{3+} sample to an overestimation of multi-phonon relaxation from the blue-emitting level in the model (Figure 2c). In addition, thermal excitation of the $^5I_4$ population might also lead to an increase of the red emission. Using the sensitivity curves of the human eye, we convert each combination of red, green, and blue intensity to a coordinate in the CIE diagram (Figure 3d), which shows a similar match between model and experiment.[40]

Based on the models of the blue, green, and red intensities (Figure 3), we can calculate the relative sensitivities of our thermometer as a function of temperature and Ho^{3+} concentration. The LIR between the red and the green emission has the largest potential for achieving a high sensitivity, since these two emissions show a strong and opposite temperature dependence at higher Ho^{3+} concentrations (Figure 3c,d). The potential of the red-to-green LIR becomes evident when we plot it against temperature (**Figure 4**a). For high Ho^{3+} concentrations, this LIR changes by approximately two orders of magnitude in the evaluated temperature range, corresponding to a relative sensitivity (Equation (1)) of S_r = 1.0% K^{-1} at 300 K.[19,20] Comparison of the calculated and the experimental ratios again confirms that our model predicts the effect of temperature and dopant concentration well with only a limited number of input parameters.

Figure 4b shows that our Ho^{3+}-based cross-relaxation thermometers offer the highest relative sensitivities at high Ho^{3+} concentrations. In fact, we achieve a superior relative sensitivity over a much wider temperature range compared to the typical Boltzmann thermometer β-$NaYF_4$:Er^{3+}.[41,42] Arguably more importantly than a high sensitivity, reliable temperature measurements require high precision, i.e., low temperature uncertainty[10] (Discussion S3, Supporting Information)

$$\delta T = \frac{1}{S_r}\frac{\sigma_{LIR}}{LIR} \tag{3}$$

Figure 4c demonstrates how the Ho^{3+} concentration affects the temperature uncertainty. While the relative sensitivity consistently increases with increasing Ho^{3+} concentration (Figure 4b), the lowest temperature uncertainty is achieved at

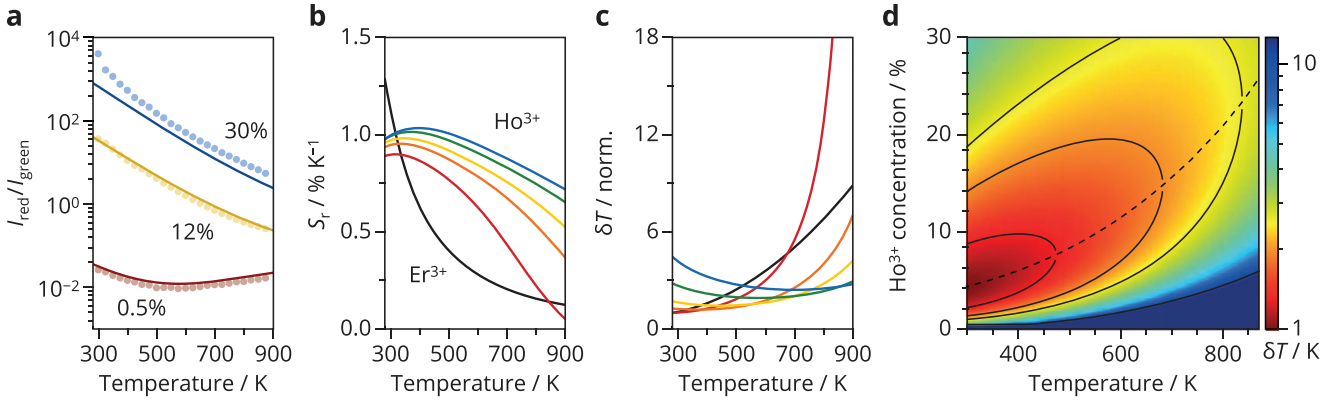

Figure 4. Evaluating thermometer performance. a) Temperature dependence of the experimentally measured (dots) and the calculated (lines) red-to-green LIR for different concentrations. The experimental red-to-green LIR was determined using the same integration boundaries as in Figure 3c,d. b) Calculated relative sensitivities for a Ho^{3+} concentration of 4% (red), 8% (orange), 12% (yellow), 20% (green), and 30% (blue), as a function of temperature. The black solid line is the relative sensitivity of the widely used Boltzmann thermometer, based on the $^4S_{3/2}$ and $^2H_{11/2}$ levels of Er^{3+} ions in the β-$NaYF_4$ host. c) Calculated temperature uncertainties (δT). The same color scheme applies as in (b). All δT values were normalized to the minimum of the curve referring to 4% Ho^{3+}. While comparing thermometers with different Ho^{3+} concentration, we account for the higher emission intensity per amount of thermometer material at higher Ho^{3+} (Discussion S3, Supporting Information). d) 3D plot of the normalized temperature uncertainty for the Ho^{3+} fractions and temperatures within the range of this study. The dashed line traces the minimum achievable δT as a function of temperature. The contour lines correspond to normalized δT values of 1.3, 1.9, 2.5, and 10.

different Ho^{3+} concentrations depending on the temperature. The trend in temperature uncertainty of our cross-relaxation thermometers becomes clearer in the color map of Figure 4d. This figure can serve as a clear guide to achieve an optimized performance of the Ho^{3+}-based luminescent thermometer over a range of 300–873 K. Around 300 K, the lowest temperature uncertainties are achieved at a Ho^{3+} concentration of 4%. At higher temperatures, a minimum temperature uncertainty requires higher Ho^{3+} concentrations, increasing by ≈1% for every 30 K step in temperature. Importantly, by choosing the optimal Ho^{3+} concentration for the temperature regime of interest, our cross-relaxation thermometers can cover the temperature range between 300 and 900 K with a consistently low temperature uncertainty, increasing by no more than a factor 2.5 over the entire range. This is a clear advantage of our temperature concept compared to Boltzmann thermometer like β-$NaYF_4$:Er^{3+}, for which the temperature uncertainty increases by as much as a factor 8.5 over this temperature range.

3. Conclusions

Our results have revealed that quantitative modeling of the decay pathways is a unique and powerful tool to evaluate the performance of luminescent thermometers based on cross-relaxation. An understanding of their concentration-dependent luminescent properties helps to adjust the design of such thermometers to the temperature regime of interest for minimum temperature uncertainty. While this work focused on cross-relaxation between Ho^{3+}, our type of modeling provides a universal tool to quantify, predict, and tune the performance of many other types of energy-transfer thermometers. This enables the rational design of new Ln^{3+}-based thermometers, but it is also indispensable in the optimization of existing energy-transfer couples.

4. Experimental Section

Chemicals: YF_3 (99.99%), HoF_3 (99.9%), and GdF_3 (99.99%) were purchased from chemPUR. NaF (≥98%) and NH_4F (≥98%) were purchased from Sigma-Aldrich. All chemicals were dried in the oven and used without further purification.

Synthesis of Microcrcystalline $NaY_{0.75-x}Gd_{0.25}Ho_xF_4$: The solid-state procedure of Aarts et al.[27] was adjusted for the synthesis of $NaY_{0.75-x}Gd_{0.25}Ho_xF_4$. As starting materials, 0.25 equiv. GdF_3, 0.75–x equiv. YF_3, x equiv. HoF_3, 1 equiv. NH_4F, and 1.2 equiv. NaF were mixed with a pestle and mortar. The ground mixture was added to an alumina crucible and placed in a tube oven, which was fired in N_2 atmosphere in an excess of NH_4F. The mixture was first heated to 300 °C for 2 h followed by an additional 10 h at 600 °C. After cooling the samples to room temperature, the powders were crushed.

Characterization: X-ray diffraction (XRD) patterns were recorded with a Philips PW1700 X-ray powder diffractometer using Cu $K_{\alpha 1}$ (λ = 1.5418 Å) radiation. The measurement range in terms of 2θ was 10°–80° with a step size of 0.02°. Using the XRD patterns, the sole presence of the hexagonal phase in the samples was confirmed and the lattice parameters ($a = b$ = 0.5973 nm, c = 0.3549 nm) were extracted (Figure S2, Supporting Information). Only minor variations in the lattice parameters were observed for samples with different Ho^{3+} concentrations. Scanning electron microscopy images were obtained using a Phenom ProX microscope with an acceleration voltage of 10 kV. Emission spectra were measured with an Edinburgh Instruments FLS920 spectrophotometer equipped with TMS300 monochromators, a R928 photomultiplier tube (PMT), and a 450 nm CW laser (1 W) or a Xe lamp (450 W) as excitation source. All emission spectra were corrected for the spectral response of the detector, monochromator, and longpass filter. Photoluminescence decay curves were recorded using an Ekspla NT342B OPO laser (10 Hz), a Triax 550 monochromator, and a Hamamatsu R928 PMT. Depending on the decay rate, the average count rate was kept at 1–50 counts per pulse to prevent detector saturation. Heating and cooling of the samples was achieved with a Linkam THMS600 microscope stage and a liquid He cooled cryostat, respectively.

Supporting Information

Supporting Information is available from the Wiley Online Library or from the author.

Acknowledgements

This work was supported by The Netherlands Center for Multiscale Catalytic Energy Conversion (MCEC), an NWO Gravitation Programme funded by the Ministry of Education, Culture, and Science of the Government of The Netherlands. F.T.R. and S.J.W.V. acknowledge financial support from The Netherlands Organisation for Scientific Research NWO (Veni-722.017.002 and OCENW.KLEIN.008). D.Y., T.Y., and Q.Z. acknowledge financial support from the National Science Foundation of China (U1601205, 51472088, and 51125005). A.M. and M.S. gratefully acknowledge funding from the EU-Horizon 2020 FET-Open project NanoTBTech (grant agreement no. 801305).

Conflict of Interest

The authors declare no conflict of interest.

Author Contributions

T.P.v.S. and D.Y. contributed equally to this work. D.Y., A.M., and F.T.R. initiated and supervised the project. D.Y., T.P.v.S., and T.Y. performed the experimental work. T.P.v.S., S.J.W.V., and F.T.R. analyzed the time-resolved spectroscopy data and constructed the model. M.S. and Q.Z. contributed to the interpretation of the results. S.J.W.V. analyzed the XRD data. T.P.v.S., M.S., and F.T.R. analyzed and discussed the thermometry concept and performance. T.P.v.S., M.S., A.M., and F.T.R. wrote the manuscript with feedback from all authors.

Keywords

cross-relaxation, holmium, lanthanide luminescence, luminescence thermometry, remote thermometry

Received: September 3, 2020
Revised: October 20, 2020
Published online: November 8, 2020

[1] T. Hartman, R. G. Geitenbeek, G. T. Whiting, B. M. Weckhuysen, *Nat. Catal.* **2019**, *2*, 986.
[2] X. Zhu, J. Li, X. Qiu, Y. Liu, W. Feng, F. Li, *Nat. Commun.* **2018**, *9*, 2176.
[3] C. D. S. Brites, X. Xie, M. L. Debasu, X. Qin, R. Chen, W. Huang, J. Rocha, X. Liu, L. D. Carlos, *Nat. Nanotechnol.* **2016**, *11*, 851.
[4] D. Ruiz, B. del Rosal, M. Acebrón, C. Palencia, C. Sun, J. Cabanillas-González, M. López-Haro, A. B. Hungría, D. Jaque, B. H. Juarez, *Adv. Funct. Mater.* **2017**, *27*, 1604629.
[5] S. Heer, K. Kömpe, H. U. Güdel, M. Haase, *Adv. Mater.* **2004**, *16*, 2102.
[6] M. Back, J. Ueda, J. Xu, K. Asami, M. G. Brik, S. Tanabe, *Adv. Opt. Mater.* **2020**, *8*, 2000124.
[7] M. D. Dramićanin, B. Milićević, V. Đorđević, Z. Ristić, J. Zhou, D. Milivojević, J. Papan, M. G. Brik, C.-G. Ma, A. M. Srivastava, M. Wu, *ChemistrySelect* **2019**, *4*, 7067.
[8] M. Sekulić, V. Đorđević, Z. Ristić, M. Medić, M. D. Dramićanin, *Adv. Opt. Mater.* **2018**, *6*, 1800552.
[9] E. N. Cerón, D. H. Ortgies, B. del Rosal, F. Ren, A. Benayas, F. Vetrone, D. Ma, F. Sanz-Rodríguez, J. G. Solé, D. Jaque, E. M. Rodríguez, *Adv. Mater.* **2015**, *27*, 4781.
[10] C. D. S. Brites, S. Balabhadra, L. D. Carlos, *Adv. Opt. Mater.* **2019**, *7*, 1801239.
[11] B. Fond, C. Abram, M. Pougin, F. Beyrau, *Opt. Mater.* **2019**, *89*, 615.
[12] A. A. Alaulamie, *Ph.D. Thesis*, College of Arts and Sciences of Ohio University, Athens, OH **2017**.
[13] R. G. Geitenbeek, H. W. De Wijn, A. Meijerink, *Phys. Rev. Appl.* **2018**, *10*, 64006.
[14] A. S. Souza, L. A. O. Nunes, I. G. N. Silva, F. A. M. Oliveira, L. L. da Luz, H. F. Brito, M. C. F. C. Felinto, R. A. S. Ferreira, S. A. Júnior, L. D. Carlos, O. L. Malta, *Nanoscale* **2016**, *8*, 5327.
[15] K. Trejgis, A. Bednarkiewicz, L. Marciniak, *Nanoscale* **2020**, *12*, 4667.
[16] C. D. S. Brites, P. P. Lima, N. J. O. Silva, A. Millán, V. S. Amaral, F. Palacio, L. D. Carlos, *Adv. Mater.* **2010**, *22*, 4499.
[17] D. Jaque, M. O. Ramirez, L. E. Bausá, J. G. Solé, E. Cavalli, A. Speghini, M. Bettinelli, *Phys. Rev. B* **2003**, *68*, 35118.
[18] X. Liu, S. Akerboom, M. de Jong, I. Mutikainen, S. Tanase, A. Meijerink, E. Bouwman, *Inorg. Chem.* **2015**, *54*, 11323.
[19] C. D. S. Brites, K. Fiaczyk, J. F. C. B. Ramalho, M. Sójka, L. D. Carlos, E. Zych, *Adv. Opt. Mater.* **2018**, *6*, 1701318.
[20] M. Runowski, P. Woźny, N. Stopikowska, I. R. Martin, V. Lavin, S. Lis, *ACS Appl. Mater. Interfaces* **2020**, *12*, 43933.
[21] E. C. Ximendes, A. F. Pereira, U. Rocha, W. F. Silva, D. Jaque, C. Jacinto, *Nanoscale* **2019**, *11*, 8864.
[22] W. T. Carnall, H. Crosswhite, H. M. Crosswhite, *Energy Level Structure and Transition Trobabilities of the Trivalent Lanthanides in LaF_3*, Argonne National Laboratory **1978**.
[23] Z. Cao, X. Wei, L. Zhao, Y. Chen, M. Yin, *ACS Appl. Mater. Interfaces* **2016**, *8*, 34546.
[24] B. Chen, Y. Liu, Y. Xiao, X. Chen, Y. Li, M. Li, X. Qiao, X. Fan, F. Wang, *J. Phys. Chem. Lett.* **2016**, *7*, 4916.
[25] H. Zou, B. Chen, Y. Hu, Q. Zhang, X. Wang, F. Wang, *J. Phys. Chem. Lett.* **2020**, *11*, 3020.
[26] Y. Hu, Q. Shao, X. Deng, J. Jiang, *Nanophotonics* **2020**, *9*, 2879.
[27] L. Aarts, B. M. der Ende, A. Meijerink, *J. Appl. Phys.* **2009**, *106*, 023522.
[28] R. S. Quimby, N. J. Condon, S. P. O'Connor, S. R. Bowman, *Opt. Mater.* **2012**, *34*, 1603.
[29] J. F. Suyver, J. Grimm, M. K. Van Veen, D. Biner, K. W. Krämer, H.-U. Güdel, *J. Lumin.* **2006**, *117*, 1.
[30] B. M. Walsh, G. W. Grew, N. P. Barnes, *J. Phys.: Condens. Matter* **2005**, *17*, 7643.
[31] M. Malinowski, R. Piramidowicz, Z. Frukacz, G. Chadeyron, R. Mahiou, M. F. Joubert, *Opt. Mater.* **1999**, *12*, 409.
[32] B. Henderson, G. F. Imbusch, *Optical Spectroscopy of Inorganic Solids*, Oxford University Press, Oxford **2006**.
[33] J. Sytsma, G. F. Imbusch, G. Blasse, *J. Phys.: Condens. Matter* **1990**, *2*, 5171.
[34] D. Yu, J. Ballato, R. E. Riman, *J. Phys. Chem. C* **2016**, *120*, 9958.
[35] K. R. German, A. Kiel, *Phys. Rev. B* **1973**, *8*, 1846.
[36] F. T. Rabouw, S. A. Den Hartog, T. Senden, A. Meijerink, *Nat. Commun.* **2014**, *5*, 3610.
[37] F. T. Rabouw, P. T. Prins, P. Villanueva-Delgado, M. Castelijns, R. G. Geitenbeek, A. Meijerink, *ACS Nano* **2018**, *12*, 4812.
[38] D. C. Yu, F. T. Rabouw, W. Q. Boon, T. Kieboom, S. Ye, Q. Y. Zhang, A. Meijerink, *Phys. Rev. B* **2014**, *90*, 165126.
[39] X. Huang, S. Han, W. Huang, X. Liu, *Chem. Soc. Rev.* **2013**, *42*, 173.
[40] M. D. Fairchild, *Color Appearance Models*, John Wiley & Sons, Chichester, UK **2013**.
[41] R. G. Geitenbeek, P. T. Prins, W. Albrecht, A. Van Blaaderen, B. M. Weckhuysen, A. Meijerink, *J. Phys. Chem. C* **2017**, *121*, 3503.
[42] G. Yao, C. Lin, Q. Meng, P. S. May, M. T. Berry, *J. Lumin.* **2015**, *160*, 276.